Supporting Information

Multifunctional Fluorine-Nitrogen Modified Carbon Quantum Dots for Enhanced Solid Polymer Electrolytes Toward Solid-State Lithium Batteries

Yang Wu, Wenbo Yue*

Beijing Key Laboratory of Energy Conversion and Storage Materials, College of Chemistry, Beijing Normal University, Beijing 100875, P. R. China

* Corresponding author

E-mail address: wbyue@bnu.edu.cn (W.B. Yue)

Experimental Section

Materials

Analytical grade of citric acid (CA, anhydrous, 99%), m-Phenylenediamine (m-PD, 99%), Formamide (FA, 99.5%), hydrofluoric acid (HF), ethanol (95%), N,N-Dimethylformamide (DMF, anhydrous, ≥99.9%) and sodium bicarbonate ($NaHCO_3$, 99%) were purchased from Aladdin. Analytical grade of lithium bis(trifluoromethanesulfonyl)imide (LiTFSI) was purchased from Duoduo Chemical Technology company. Analytical grade of conductive carbon (super P), N-methylpyrrolidone (NMP), poly(vinylidene fluoride-co-hexafluoropropylene) (PVDF-HFP, Mw = ~600,000) and polyvinylidene fluoride (PVDF) were purchased from Sigma-aldrich. Analytical grade of 1-Allyl-2,3-dimethylimidazolium chloride (AmimCl), lithium Iron(II) phosphate (LFP) and lithium cobalt oxide (LCO) were purchased from Adamas. Analytical grade of lithium nickel cobalt manganese oxide (NCM811) and lithium metal electrode sheet was purchased from Canrd Technology company. Deionized (DI) water was obtained from the laboratory ultrapure water device. Unless otherwise specified, the above purchased reagents used in the experiments have not been further purified.

Materials characterization

All characterization tests were performed on sections taken from the same large polymer electrolyte film to ensure consistency. The morphology was investigated by Field- emission scanning electronic microscope (SEM) on a Thermo Fisher Helios G4 CX electron microscope at an accelerating voltage of 5-10 kV. Transmission electron microscopy (TEM) and high-resolution TEM (HRTEM) were performed to observe the fine microstructure on a FEI Talos F200S electron microscope operated at an accelerating voltage of 200 kV. X-ray power diffraction (XRD) was performed to obtain the crystalline structure of samples by using a Phillips X'pert Pro MPD diffractometer with Cu K_α radiation. Fourier transform infrared (FT-IR) spectra from 500-4000 cm^{-1} were acquired on an ALPHA II (BRUKER, Germany) spectrometer. The X-ray photoelectron spectroscopy (XPS) measurement was conducted on a

Shimadzu Axis Ultra spectrometer with an Mg K_α excitation source. XPS depth profiling uses argon ion sputtering with a sputtering rate of 0.2 nm s^{-1}. The Raman spectroscopy test was carried out by Thermo Fischer DXR with a laser wavelength of 633 nm. The differential scanning calorimeter (DSC) analysis was performed using a NETZSCH 3500 instrument under a nitrogen atmosphere at a heating rate of 10 °C min^{-1}. The stress-strain curves and corresponding mechanical properties were determined using a AGX-V 500N instrument. The test was performed on dumbbell-shaped samples at a stretching speed of 50 mm min^{-1}. Thermogravimetric analysis (TGA) was measured in N_2 atmosphere at a heating rate of 10 ℃ min^{-1}. Solid-state NMR spectra were acquired on a JEOL JNM-ECZL600G spectrometer. The ^{19}F NMR spectrum was recorded at a resonance frequency of 564.17 MHz with a spinning speed of 15 kHz, 128 scans and a relaxation delay of 1 s. The ^{7}Li NMR spectrum was obtained at a resonance frequency of 233.02 MHz under the same spinning speed of 15 kHz, with 100 scans and a relaxation delay of 0.5 s.

Performance measurements

The LFP cathode slurry was prepared by mixing $LiFePO_4$ active material, Super P conductive carbon, and poly(vinylidene fluoride) (PVDF) binder at a mass ratio of 8:1:1 in an appropriate amount of N-methyl-2-pyrrolidone (NMP) solvent. The mixture was vigorously ground in an agate mortar to form a homogeneous slurry. The resulting slurry was uniformly coated onto a carbon-coated aluminum foil current collector using a doctor blade. The coated electrode was then transferred to a vacuum oven and dried at 60 °C for 24 h to remove the residual solvent. After drying, the electrode film was calendered (rolled) to improve particle contact and then punched into circular discs with a diameter of 9 mm for use as the cathode. Following the same slurry preparation and electrode fabrication procedure, LCO and NCM811 cathodes were also prepared by using $LiCoO_2$ and $LiNi_{0.8}Co_{0.1}Mn_{0.1}O_2$ as the active material, respectively.

All battery assembly and disassembly procedures were performed in a glove box with water and oxygen levels maintained below 0.01 ppm. The assembly of CR2032 coin cells (lithium symmetric, stainless steel symmetric, and full cells) was carried out by

sandwiching the circular polymer electrolyte film between two lithium electrodes, two stainless steel sheets, or a lithium anode and a cathode. The electrolyte diameter always slightly exceeded that of the electrodes to avoid short circuits. The mass loadings of the active materials (LFP, LCO, NCM811) were 2.81, 3.03, and 3.37 mg cm^{-2}, respectively. For the high-loading LFP cathode, the active material mass loading was increased to 6.09 mg cm^{-2}. All battery tests were conducted at room temperature (25 °C). The packing densities of the LFP, LCO and NCM811 electrodes were 2.34, 3.94 and 3.51 g cm^{-3}, respectively. The lithium anode used in our experiments is excessive, so the N/P ratio is considered infinite. The thickness of the electrolyte membranes is approximately 67 μm. The coin cells were tested under the intrinsic pressure provided by the wave spring inside the CR2032 case, without additional external stacking pressure. All fabrication and testing conditions for the full-cells were kept consistent to exclude the influence of factors other than the electrolyte.

Linear sweep voltammetry (LSV) and electrochemical impedance spectroscopy (EIS) measurements was performed on a Gamry Interface 1000 electrochemical station. The LSV profiles were obtained between 2 and 6 V in a sweep rate of 4 mV S^{-1}. The impedance spectra were acquired with an applied AC amplitude of 10 mV over a frequency range from 0.1 Hz to 1 MHz, all carried out at room temperature. The ionic conductivity (σ) is calculated by equation (1):

$$\sigma = \frac{d}{R_e \times S} \qquad (1)$$

In the equation, d represents the thickness of the tested sample (cm); R_e is the bulk impedance (ohm) of the tested sample; S represents the effective contact area (cm^2) between the electrode and the polymer electrolyte.

The determination of the lithium-ion transference number (t_{Li^+}) was performed by DC polarization coupled with impedance analysis. Specifically, a constant potential of 10 mV was applied to a Li||Li symmetric cell and the current was tracked via chronoamperometry. Impedance measurements were taken before and after polarization, enabling the calculation via equation (2):

$$t_{Li+} = \frac{I_s(\triangle V - I_0 R_0)}{I_0(\triangle V - I_s R_s)} \quad (2)$$

In the equation, ΔV represents the applied constant potential, while I_0 and I_s denote the initial and steady-state currents, and R_0 and R_s represent the initial and steady-state resistances after polarization, respectively.

The galvanostatic charge-discharge tests were conducted in the voltage range of 2.4 to 4.0 V for LFP cathode, 2.8 to 4.3 V for LCO cathode and NCM811 cathode (vs. Li/Li^+) on a Neware test system at room temperature.

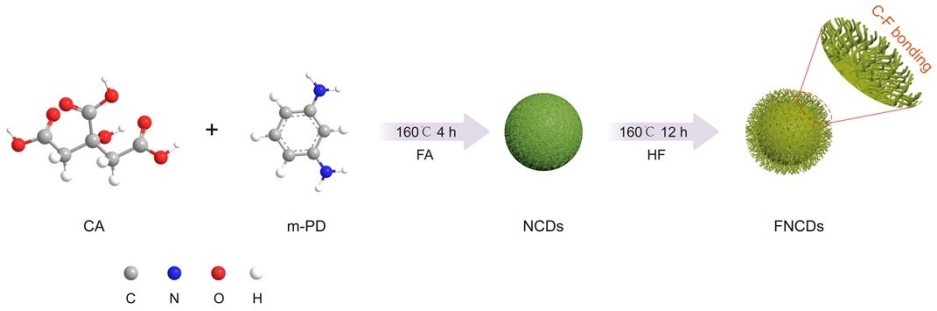

Fig. S1 Schematic illustration of the synthetic route of NCDs and FNCDs.

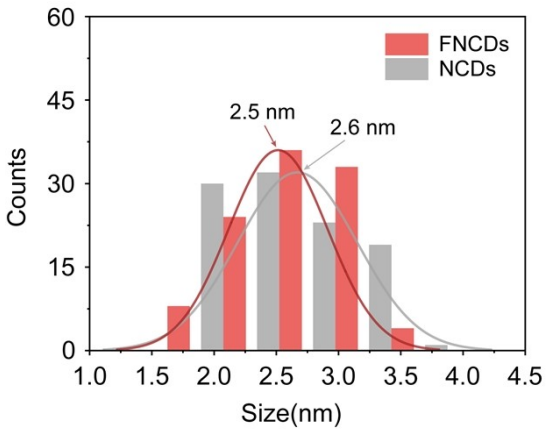

Fig. S2 Particle size distribution histograms of NCDs and FNCDs.

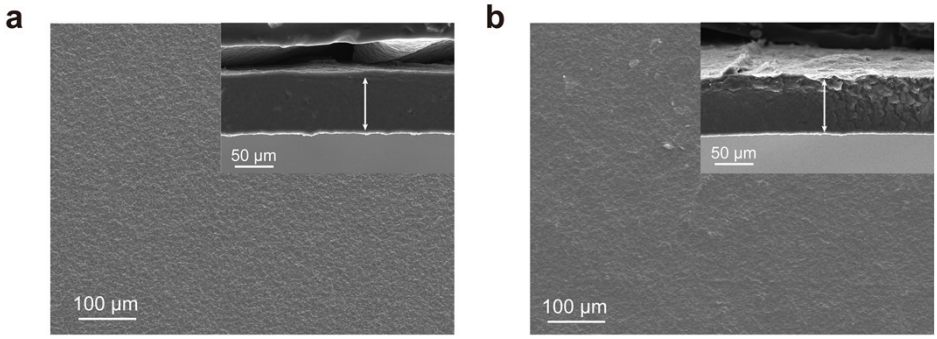

Fig. S3 SEM images of (a) NCDs-SPE and (b) P-SPE films. The insets of (a) and (b) are the cross-sectional SEM images, respectively. The thickness of NCDs-SPE and P-SPE is approximately 67 μm.

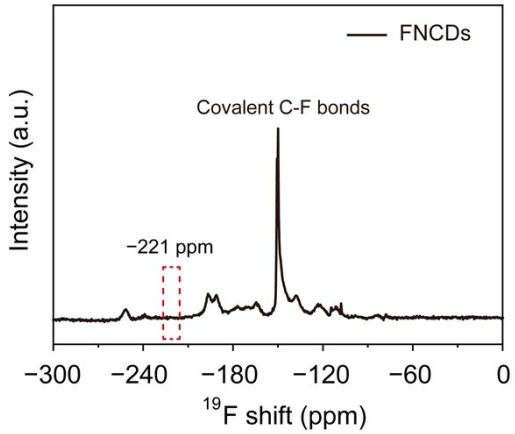

Fig. S4 The solid-state ^{19}F NMR spectrum of FNCDs.

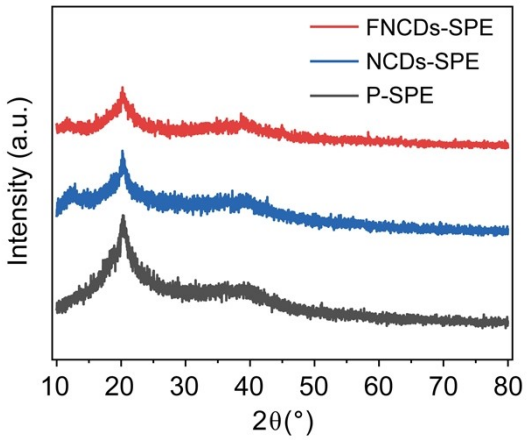

Fig. S5 XRD patterns of FNCDs-SPE film, NCDs-SPE film and P-SPE film.

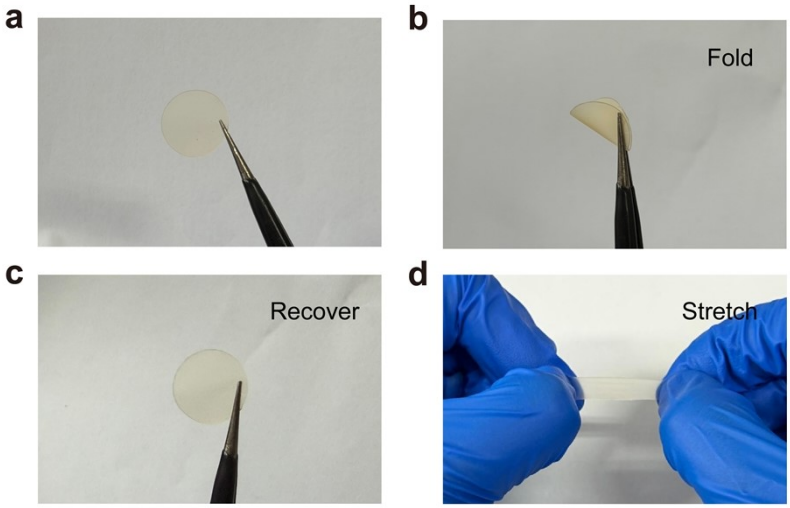

Fig. S6 The optical photograph of FNCDs-SPE film under condition of (a) normal, (b) fold, (c) recover after fold and (d) stretch.

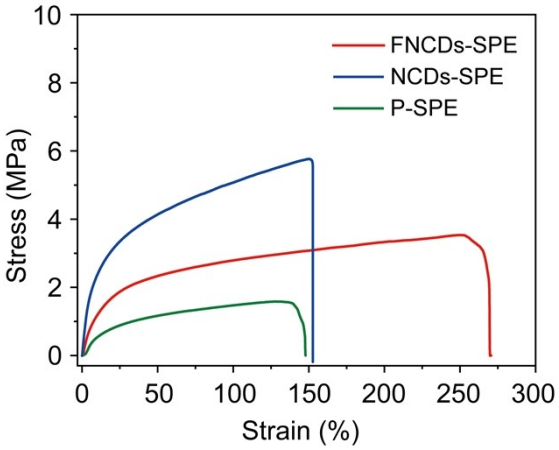

Fig. S7 The stress-strain curves of FNCDs-SPE film, NCDs-SPE film and P-SPE film.

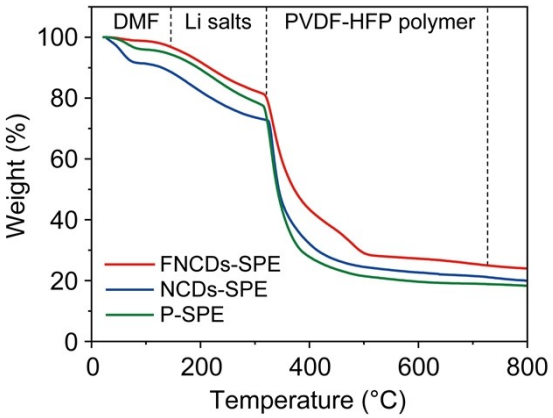

Fig. S8 The TGA curves of FNCDs-SPE film, NCDs-SPE film and P-SPE film. It mainly includes the following three stages: (1) Slight mass loss is attributed to the evaporation of residual DMF solvent; (2) Thermal decomposition of LiTFSI; (3) Chain breakage and gradual decomposition of polymer PVDF-HFP.

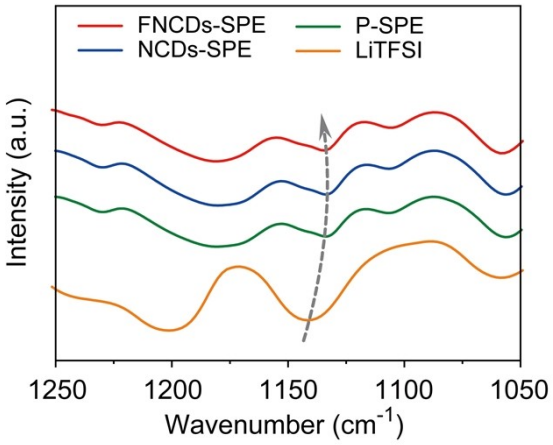

Fig. S9 FT-IR spectra of FNCDs-SPE film, NCDs-SPE film, P-SPE film and LiTFSI.

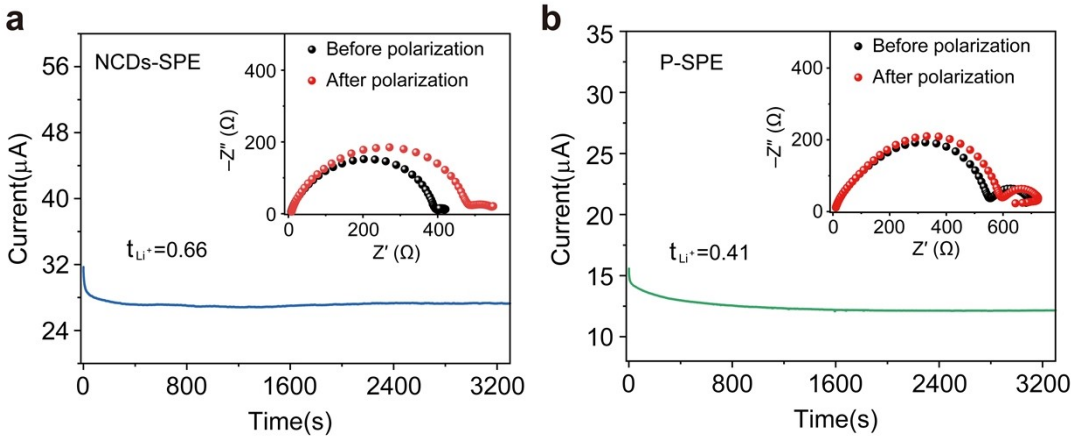

Fig. S10 Polarization curves of (a) Li||NCDs-SPE||Li and (b) Li||P-SPE||Li cells (inset: the impedance diagram before and after polarization).

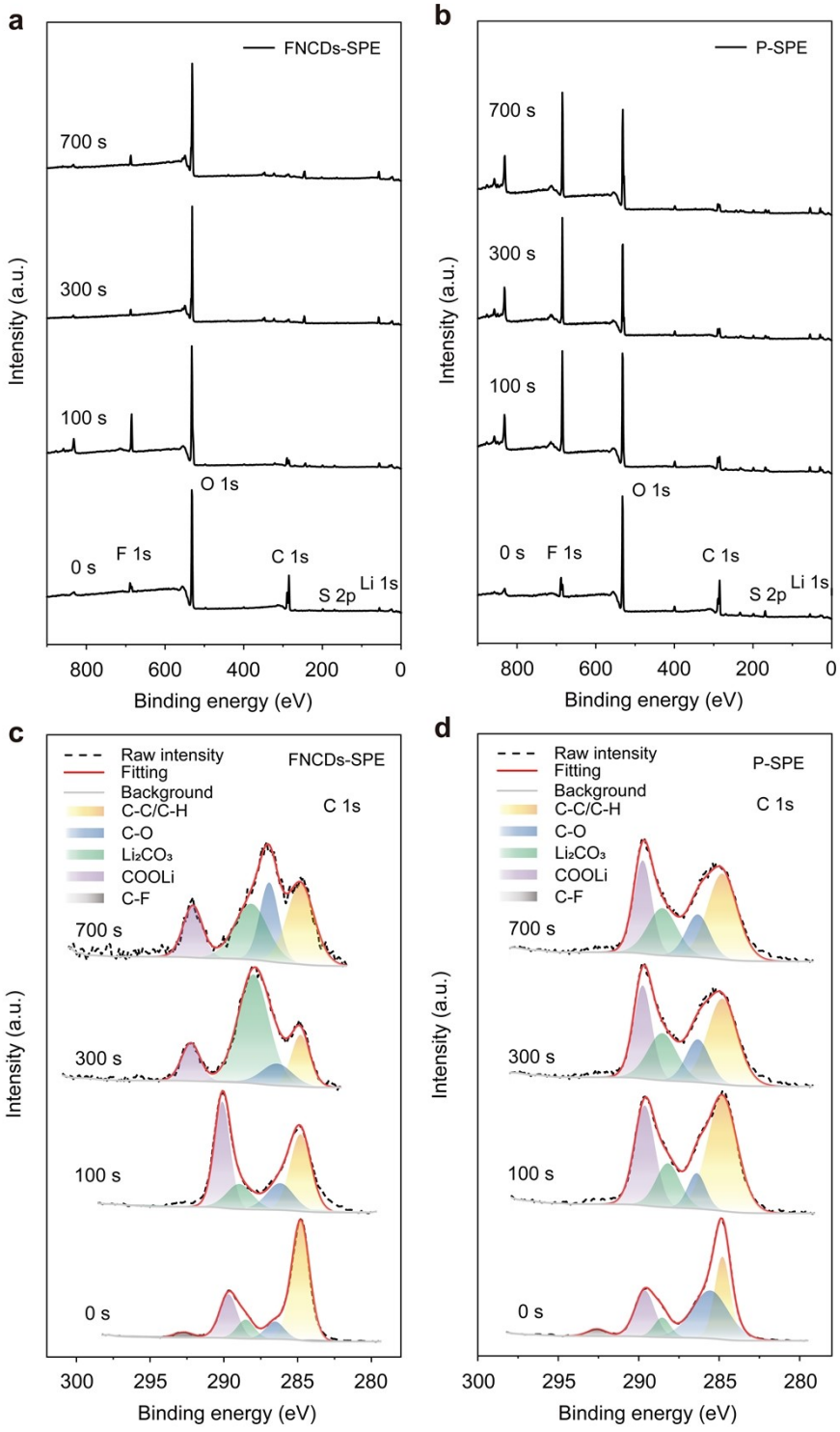

Fig. S11 XPS depth profiles of the survey and C 1s spectra for (a,c) FNCDs-SPE and (b,d) P-SPE.

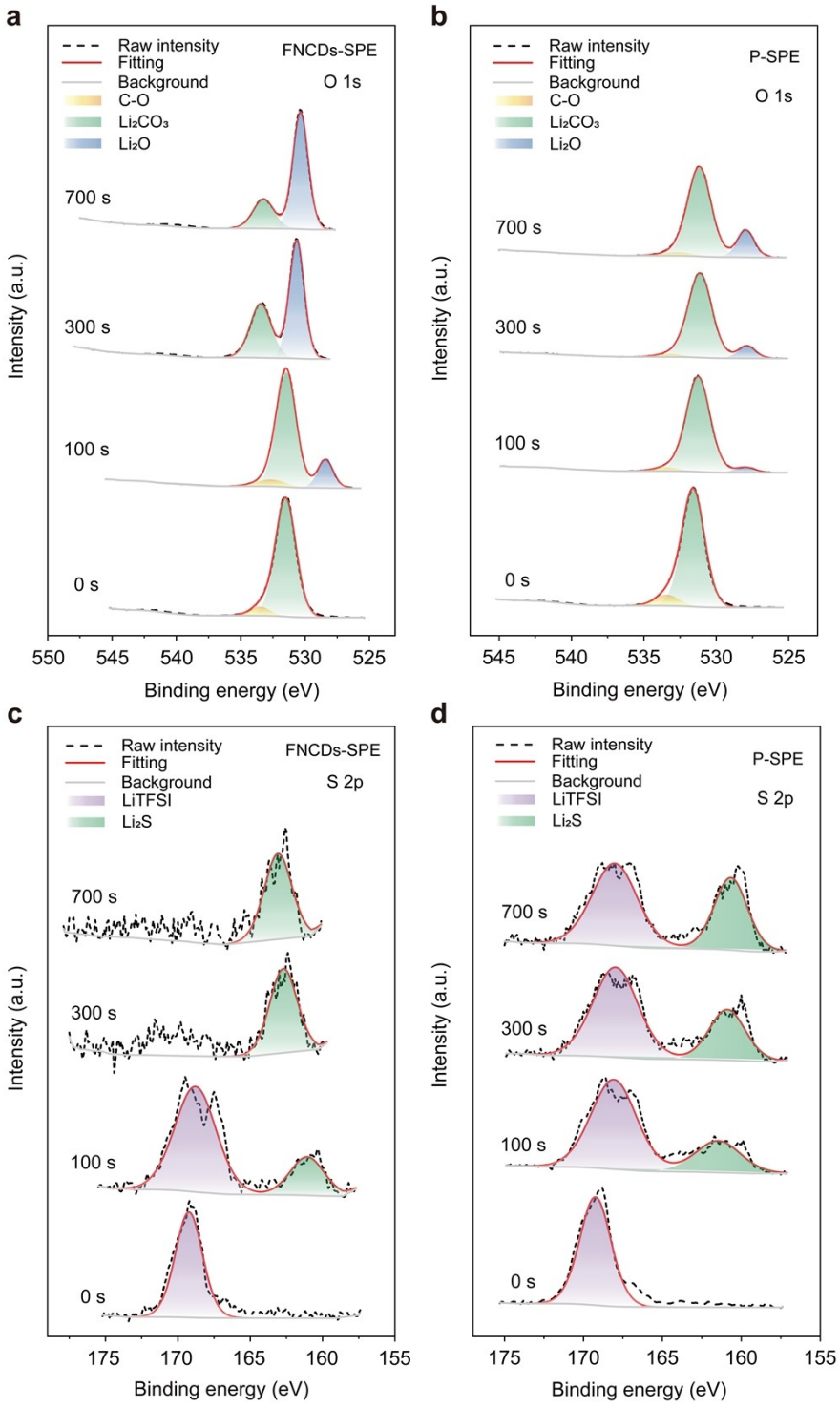

Fig. S12 XPS depth profiles of the O 1s and S 2p spectra for (a,c) FNCDs-SPE and (b,d) P-SPE.

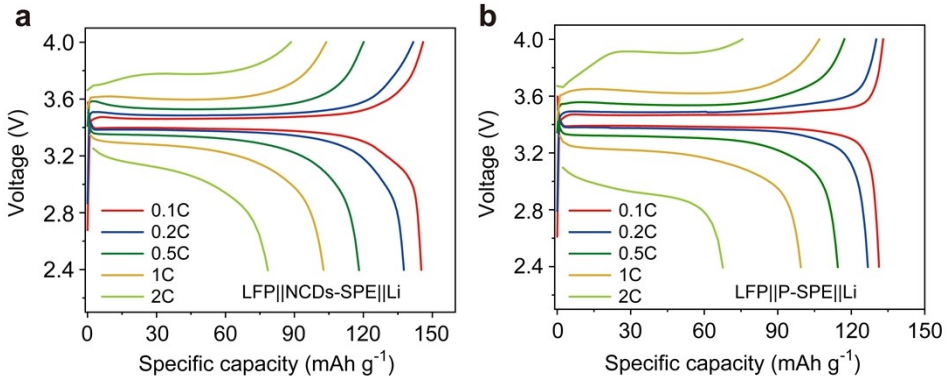

Fig. S13 The charge/discharge curves of (a) LFP||NCDs-SPE||Li and (b) LFP||P-SPE||Li cells at different current densities.

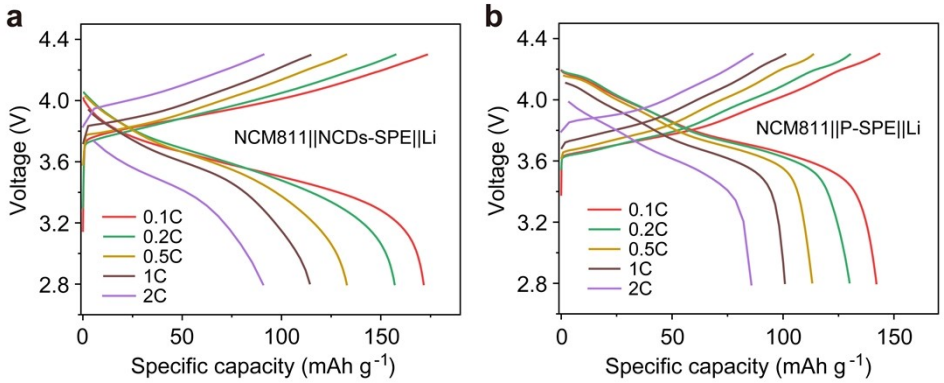

Fig. S14 The charge/discharge curves of (a) NCM811||NCDs-SPE||Li and (b) NCM811||P-SPE||Li cells at different current densities.

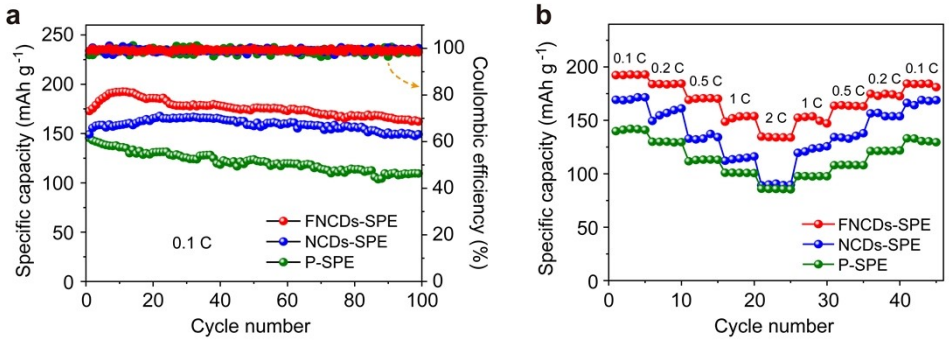

Fig. S15 (a) The cycling performance at 0.1 C and (b) rate performance at 0.1-2 C of NCM811||FNCDs-SPE||Li, NCM811||NCDs-SPE||Li and NCM811||P-SPE||Li cells.

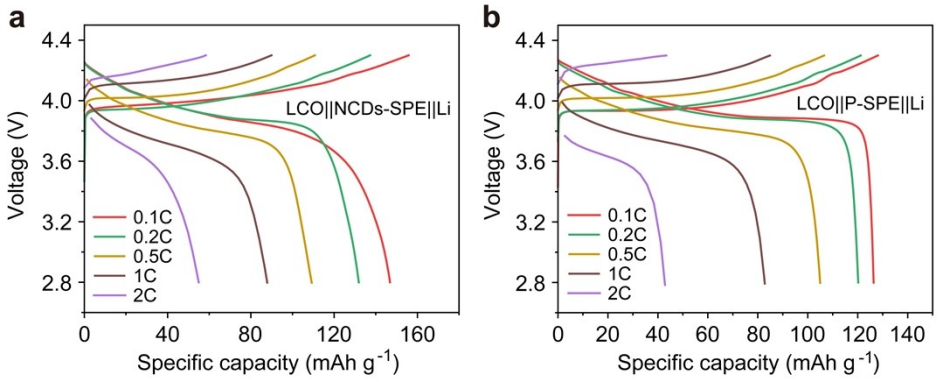

Fig. S16 The charge/discharge curves of (a) LCO||NCDs-SPE||Li and (b) LCO||P-SPE||Li cells at different current densities.

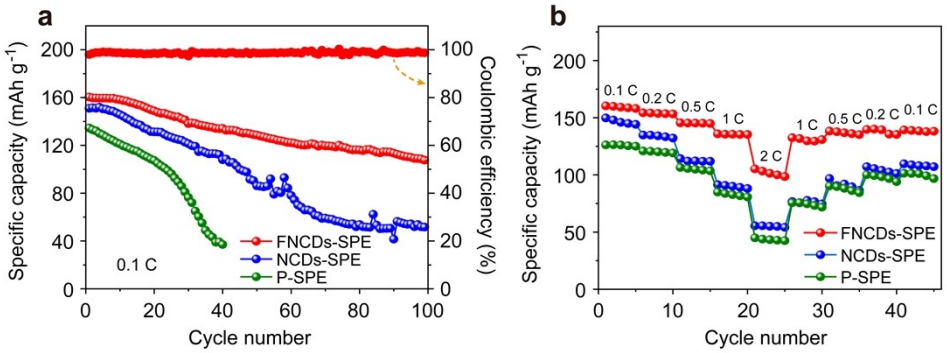

Fig. S17 (a) The cycling performance at 0.1 C and (b) rate performance at 0.1-2 C of LCO||FNCDs-SPE||Li, LCO||NCDs-SPE||Li and LCO||P-SPE||Li cells.

Table S1 Mechanical performance of the three electrolytes.

Sample	Tensile strength (kPa)	Elongation at break (%)	Elastic modulus (kPa)
FNCDs-SPE	3535.8	249.2	7096.2
NCDs-SPE	5767.2	150.3	55713.3
P-SPE	1583.5	128.1	3799.1

Table S2 Various numerical values for calculating ionic conductivity.

Sample	d (cm)	R_e (Ω)	S (cm^2)	σ (S cm^{-1})
FNCDs-SPE	0.0067	6.18	1.13	0.000959418
NCDs-SPE		14.10		0.000420511
P-SPE		43.40		0.000136618

Table S3 Various numerical values for calculating lithium-ion transference number.

Sample	I_0 (A)	I_S (A)	R_0 (Ω)	R_S (Ω)	ΔV	t_{Li^+}
FNCDs-SPE	0.00001569	0.00001376	519.53	574.45	0.01	0.773625263
NCDs-SPE	0.00003169	0.00002728	388.23	476.47		0.661258639
P-SPE	0.00001561	0.00001215	545.73	593.42		0.413216679

Table S4 Comparison with the recently published work related to polymer electrolytes.

Material	σ (S cm^{-1})	t_{Li^+}	Tensile strength (MPa)	Voltage window (V)	Ref.
CP-SSE	1.09×10^{-3}	0.81	12	4.5	[1]
PEO/P-FCD	7.5×10^{-5}	0.48	3.53	4.8	[2]
CF_3-COF@ PVDF-HFP	1.21×10^{-3}	0.77	1.58	4.85	[3]
TDCT-7.2%	2.5×10^{-4}	0.79	15	5.3	[4]
T-SPE	9×10^{-4}	0.56	0.11	5.6	[5]
PELT	1.2×10^{-4}	0.46	1.1	4.9	[6]
PAN fiber-PEGDA	8.8×10^{-4}	0.42	5.62	4.8	[7]
FNCDs-SPE	9.59×10^{-4}	0.77	3.54	4.93	This work

References

[1] Li, J. et al. Molecular engineering of renewable cellulose biopolymers for solid-state battery electrolytes. Nat. Sustain. 2024, 7, 1481-1491.

[2] Xu, L. et al. Molecular engineering of highly fluorinated carbon dots: tailoring Li^+ dynamics and interfacial fluorination for stable solid lithium batteries. ACS Nano 2023, 17, 22082-22094.

[3] Feng, G. et al. Designing cooperative ion transport pathway in ultra-thin solid-state electrolytes toward practical lithium metal batteries. Angew. Chem. Int. Edit. 2025, 64, e202413306.

[4] Yang, B. et al. Super-Ionic Conductor Soft Filler Promotes Li^+ Transport in Integrated Cathode–Electrolyte for Solid-State Battery at Room Temperature. Adv. Mater. 2024, 36, 2403078.

[5] Han, J. et al. Fluorine-containing phase-separated polymer electrolytes enabling high-energy solid-state lithium metal batteries. Adv. Funct. Mater. 2024, 34, 2310801.

[6] Liu, X. et al. LATP-Enhanced Polymer Electrolyte for an Integrated Solid-State Battery. Polymers 2025, 17, 2673.
[7] Zhang, Y. et al. Fiber-reinforced ultrathin solid polymer electrolyte for solid-state lithium-metal batteries. Adv. Funct. Mater. 2025, 35, 2421054.